A Reusable Launcher Benchmark with Advanced Recovery Guidance*

P. Simplício, A. Marcos and S. Bennani

Abstract The current interest on launcher reusability has led to several mission optimisation studies aiming to maximise payload while meeting tight aerothermal constraints. However, in this article it is shown that further benefits can be achieved by jointly addressing the tasks of vehicle dimensioning and guidance and control design. To enable this approach, a thorough understanding of reusable flight mechanics and of its fundamental guidance and control interactions is necessary. This can only be accomplished by using a benchmark specifically accounting for these couplings. This article presents such a benchmark, which is capable of simulating the launch and recovery of a vertical take-off and landing booster used as a first stage of a lightweight, non-winged vehicle, steered via thrust vector control, fins and cold gas thrusters. In addition, and based on the joint dimensioning/design assessment and developed benchmark, a guidance algorithm for retro-propulsive entry, descent and pinpoint landing based on successive convex optimisation is proposed. Comparable algorithms exist in the literature, but they tend to focus on maximising either computational efficiency (typically disregarding aerodynamic deceleration) or trajectory optimality (employing multiple convex approximations). Moreover, they are targeted to low-altitude and low-velocity flight, which is not representative of launchers. The proposed algorithm intends to provide a middle ground between efficiency and optimality that is specifically tailored to the extended flight envelope encountered by reusable launchers, and is therefore termed *DESCENDO* (Descending over Extended Envelopes using Successive Convexification-based Optimisation). Its effectiveness is verified in a closed-loop fashion using complete recovery scenarios included in the reusable launcher benchmark.

P. Simplício and A. Marcos
Technology for Aerospace Control, University of Bristol, Bristol BS8 1TR, UK,
e-mail: pedro.simplicio/andres.marcos @bristol.ac.uk

S. Bennani
ESA ESTEC, Noordwijk 2200, The Netherlands, e-mail: samir.bennani@esa.int

1 Introduction

The potential benefits and technical feasibility of launcher reusability as a key paradigm for sustainable access to Space have been clearly demonstrated by private companies (i.e. SpaceX and Blue Origin with the successful vertical take-off and vertical landing (VTVL) of reusable boosters [6]). From these private industry demonstrations, recent programmes in the US and in Europe have started recently to study this paradigm [9, 8, 31, 26, 12]. The core aim of these studies lies on the application of a multi-disciplinary optimisation (MDO) framework to determine combined launch and recovery (L&R) reference trajectories, staging conditions and preliminary vehicle configurations that allow to reach the highest payload while keeping aerodynamic and thermal loads at reasonable levels.

In complement to these efforts, but using a very different perspective to MDO, a European Space Agency sponsored activity is studying other efficient design frameworks to manage these requirements based on advanced closed-loop recovery guidance algorithms and robust attitude control. In order to carry out this activity, a more complete understanding of reusable flight mechanics and of the interactions with guidance and control (G&C) algorithms and mechanisms is fundamental. This becomes even more relevant for the next-generation of launchers, where more flexible structures lead to stronger aeroelastic couplings between control-induced loads, wind perturbations and rigid-body motion [28, 20].

In this article, the development of a nonlinear 6 degrees-of-freedom benchmark model is presented. The main goal of this benchmark is the assessment of reusable launcher G&C approaches – taking into account their complex couplings as well as those arising from flight mechanics. It simulates the L&R trajectory of a mixed-fuel VTVL booster used as first stage of a lightweight, non-winged launcher injecting a 1,100 kg satellite in a quasi-polar orbit at 800 km. Two recovery scenarios are addressed: downrange landing (DRL) and return to launch site (RTLS).

Furthermore, a guidance algorithm for retro-propulsive entry, descent and pinpoint landing based on online successive convex optimisation is proposed. Though comparable in strategy, successive convexification algorithms found in literature [30, 17, 29] differ mainly in their aim of increasing computational efficiency or reaching trajectory design optimality. Moreover, their coverage is confined to mild conditions and does not hold when the operational dynamics of reusable launchers is incorporated. The *DESCENDO* (Descending over Extended Envelopes using Successive Convexification-based Optimisation) algorithm has been designed as a middle-ground between efficiency and optimality and is specifically tailored to the dynamics in which reusable launchers operate.

The article is organised as follows: Sec. 2 describes the building blocks of the benchmark model, Sec. 3 introduces the L&R mission scenarios and the *DESCENDO* algorithm, and Sec. 4 illustrates the most relevant flight simulation results.

2 RLV Flight Mechanics Modelling

The reusable launch vehicle (RLV) flight mechanics model results from the interconnection of several system sub-components. The main blocks are depicted in Fig. 1 and summarised in the following subsections.
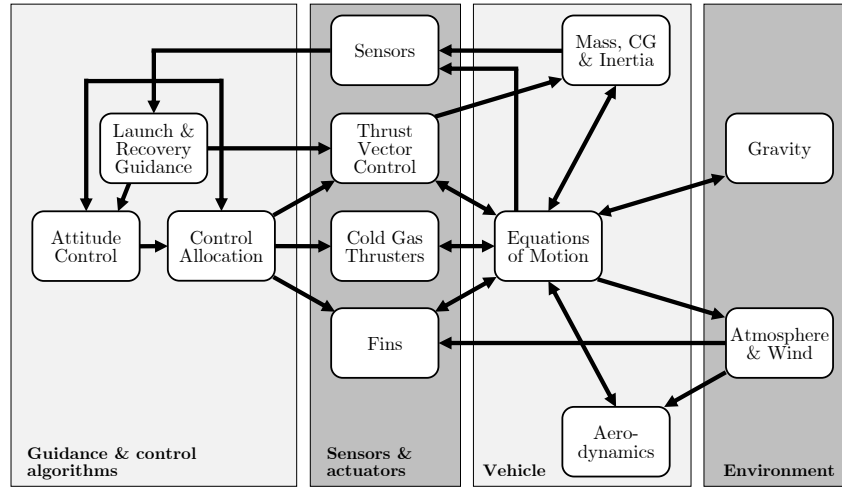
Fig. 1: RLV Simulation block interconnections

Reference frames and environment models are briefly presented in Sec. 2.1. A detailed description of aerodynamic calculations and mass, CG & inertia (MCI) evolution is provided in Sec. 2.2 and 2.6. The vehicle is mainly steered via thrust vector control (TVC), but two pairs of fins are also included to provide attitude control under low thrust and two pairs of cold gas thrusters for low dynamic pressure conditions. These actuators are introduced in Sec. 2.3, 2.4 and 2.5.

Guidance and control (G&C) algorithms are then organised in three subsystems. The first one, "launch & recovery (L&R) guidance", is responsible for the online generation of thrust and attitude commands. A dedicated discussion on L&R mission profiles and guidance is provided in Sec. 3. The "attitude control" subsystem is responsible for the computation of attitude control moments and the "control allocation" subsystem for the allocation among the aforementioned actuators.

The latter two functions are outside the scope of this article and are detailed in [25]. The reader is also referred to this reference for further information on any of the remaining sub-components (e.g. equations of motion).

2.1 Reference Frames & Environment

The first reference frame to be used is the Earth-Centred Inertial (ECI) frame, with basis vectors $\{\mathbf{i}_I, \mathbf{j}_I, \mathbf{k}_I\}$. Its origin is at the centre of the Earth, $\mathbf{i}_I$ points to the vernal equinox, $\mathbf{k}_I$ to the North pole and $\mathbf{j}_I$ completes a right-handed set. Since the Earth's orbital motion around the Sun can be neglected for the study of RLV trajectories, the ECI frame is considered inertial and the equations of motion are referred to it.

With the same origin and equatorial plane, the Earth-Centred Earth-Fixed (ECEF) frame is defined by the set of vectors $\{\mathbf{i}_E, \mathbf{j}_E, \mathbf{k}_E\}$. This frame rotates with the

Earth's angular velocity $\Omega_I = \omega_E \mathbf{k}_I$, keeping $\mathbf{i}_E$ along the Greenwich meridian. It is useful for the computation of position-dependent quantities due to a straightforward conversion between its coordinates and latitude, longitude and altitude $\{\varphi(t), \lambda(t), h(t)\}$.

In this study, simulations are initiated from the European Space Centre situated in French Guiana [16], with $\{\varphi(0), \lambda(0), h(0)\} \approx \{5.2 \text{ deg}, -52.8 \text{ deg}, 0 \text{ m}\}$. Defining this initial position in the ECI frame as $\mathbf{r}_I(0)$, the initial velocity of the vehicle due to the Earth's rotation is $\mathbf{v}_I(0) = \Omega_I \times \mathbf{r}_I(0)$. Furthermore, the rotation quaternion $\mathbf{q}_E^I(t)$ from ECI to ECEF and the associated Direction Cosine Matrix (DCM) $C_{\mathbf{q}_E^I}(t)$ are related to their initial values as follows:

$$C_{\mathbf{q}_E^I}(t) = \begin{bmatrix} \cos\omega_E t & \sin\omega_E t & 0 \\ -\sin\omega_E t & \cos\omega_E t & 0 \\ 0 & 0 & 1 \end{bmatrix} C_{\mathbf{q}_E^I}(0) \tag{1}$$

For a more intuitive analysis of launch trajectories, the Launch Pad (LP) reference frame is fixed at the initial position $\mathbf{r}_I(0)$ and specified by $\{\mathbf{i}_L, \mathbf{j}_L, \mathbf{k}_L\}$. Here, $\mathbf{k}_L$ is normal to the local horizon, $\mathbf{i}_L$ indicates the direction of launch, with an azimuth χ relative to the North, and $\mathbf{j}_L$ completes a right-handed set. The reference mission addressed in this study (see Sec. 3.1) is based on a satellite injection in a quasi-polar orbit, with $\chi \approx -0.02$ degrees. Equivalently, vectors specifying a Recovery Pad (RP) reference frame $\{\mathbf{i}_R, \mathbf{j}_R, \mathbf{k}_R\}$ are defined in the same way, but having the origin at a recovery platform position, which may or may not coincide with the launch pad.

The transformations between ECEF and local frames, $C_{\mathbf{q}_L^E}$ and $C_{\mathbf{q}_R^E}$, are time-invariant and of straightforward computation [2]. To determine the position and velocity relative to the LP frame, its origin and the contribution of the Earth's rotation must be accounted for as follows:

$$\begin{cases} \mathbf{r}_L(t) = C_{\mathbf{q}_L^E} C_{\mathbf{q}_E^I}(t) \left[\mathbf{r}_I(t) - \mathbf{r}_I(0)\right] \\ \mathbf{v}_L(t) = C_{\mathbf{q}_L^E} C_{\mathbf{q}_E^I}(t) \left[\mathbf{v}_I(t) - \Omega_I \times \mathbf{r}_I(t)\right] \end{cases} \tag{2}$$

with $C_{\mathbf{q}_E^I}(t)$ given by Eq. (1), and in the same way for the RP frame.

Then, the vehicle's body-fixed reference frame is fixed to its centre of gravity (CG) and has basis vectors $\{\mathbf{i}_B, \mathbf{j}_B, \mathbf{k}_B\}$. Vector $\mathbf{i}_B$ lies along the vehicle's longitudinal axis and $\mathbf{j}_B$ is defined so as to remain perpendicular to the trajectory plane and have a positive pitch angle.

Following this definition, roll, pitch and yaw angles $\{\phi(t), \theta(t), \psi(t)\}$ measure the spin of the longitudinal axis $\mathbf{i}_B$, and its angular deflection about the LP horizon and pitch plane, respectively. Hence, upon launch, $\{\phi(0), \theta(0), \psi(0)\} = \{\pi, \frac{\pi}{2}, 0\}$ radians, the inertial orientation of the vehicle's body is given by:

$$C_{\mathbf{q}_B^I}(0) = \begin{bmatrix} 0 & 0 & 1 \\ 0 & -1 & 0 \\ 1 & 0 & 0 \end{bmatrix} C_{\mathbf{q}_L^E} C_{\mathbf{q}_E^I}(0) \tag{3}$$

and its initial angular velocity corresponds to $\omega_B(0) = C_{\mathbf{q}_B^I}(0)\,\Omega_I$. The offset between launch pad and the vehicle's CG can be neglected for practical computations.

The ECI and body-fixed frames are employed to write the equations of motions, whose derivations can be found in [15] and [13]. They are based on the initial states $\{\mathbf{r}_I(0), \mathbf{v}_I(0), \mathbf{q}_B^I(0), \omega_B(0)\}$ and on the assumption that effects related to MCI time-derivatives ($\dot{m}$ and $\dot{J}$, see Sec. 2.6) and moving masses (including "tail-wags-dog" moment and rocket jet damping) are negligible for trajectory assessment. The orientation of the vehicle's body axes in the ECI frame, $C_{\mathbf{q}_B^I}(t)$, is propagated through the kinematics of quaternion $\mathbf{q}_B^I(t)$.

For the computation of the aerodynamic characteristics, a velocity reference frame (VRF) is defined using using vectors $\{\mathbf{i}_V, \mathbf{j}_V, \mathbf{k}_V\}$. This frame is also fixed to the vehicle's CG, but now with $\mathbf{i}_V$ directed along the air-relative velocity vector $\mathbf{v}_{air}(t)$. A vector rotation from the body-fixed to VRF, $C_{\mathbf{q}_V^B}(t)$, can be represented by two aerodynamic angles, the angle of attack $\alpha(t)$ and sideslip $\beta(t)$.

The gravity model adopted in this study is the Earth Gravitational Model [21] (EGM), which is based on a spherical harmonic representation of the gravity field and implemented in [2]. It contains a function $\mathbf{g}_{EGM}$ that computes the gravity acceleration in the ECEF frame. Hence, the corresponding vector in inertial coordinates is given by:

$$\mathbf{g}_I(t) = C_{\mathbf{q}_I^E}(t) \, \mathbf{g}_{EGM} \left(C_{\mathbf{q}_E^I}(t) \, \mathbf{r}_I(t) \right) \tag{4}$$

The atmosphere model adopted is also available in [2] and implements the mathematical representation of the 1976 Committee on Extension to the Standard Atmosphere [1] (COESA). This representation provides, as a function of altitude, the air density $\rho(h(t))$ and the speed of sound $a(h(t))$.

Finally, wind gusts are included by adding an altitude-dependent velocity field with Northern and Eastern components $\{w_{NRN}(h(t)), w_{ERN}(h(t))\}$ relative to LP. These components can be generated using, for example, traditional Dryden filters. The wind perturbation with respect to the ECEF frame then corresponds to:

$$\mathbf{w}_E(t) = C_{\mathbf{q}_E^L} \begin{bmatrix} \cos\chi & \sin\chi \\ \sin\chi & -\cos\chi \\ 0 & 0 \end{bmatrix} \begin{bmatrix} w_{NRN}(h(t)) \\ w_{ERN}(h(t)) \end{bmatrix} \tag{5}$$

2.2 Aerodynamics Characteristics

Aerodynamic forces and moments generated by the vehicle's main body depend on its external shape, as well on the instantaneous dynamic pressure. Assuming that the Earth's atmosphere rotates with the planet without slippage and shearing, dynamic pressure is given by:

$$Q(t) = \frac{1}{2}\rho(t) \|\mathbf{v}_{air}(t)\|^2 \tag{6}$$

where $\mathbf{v}_{air}(t) = [v_{air,x}(t); v_{air,y}(t); v_{air,z}(t)]$ is the air-relative velocity vector written in the body-fixed frame. This vector accounts for the vehicle's inertial velocity $\mathbf{v}_I(t)$, Earth's rotation Ω_I and wind gusts $\mathbf{w}_E(t)$ as follows:

$$\mathbf{v}_{air}(t) = C_{\mathbf{q}_B^I}(t) \left[\mathbf{v}_I(t) - \Omega_I \times \mathbf{r}_I(t) - C_{\mathbf{q}_I^E}(t) \, \mathbf{w}_E(t) \right] \tag{7}$$

and allows to define the aerodynamic angles:

$$\alpha(t) = \arctan_2 \frac{v_{\text{air,z}}(t)}{v_{\text{air,x}}(t)}; \qquad \beta(t) = \arcsin \frac{v_{\text{air,y}}(t)}{\|\mathbf{v}_{\text{air}}(t)\|} \tag{8}$$

The vehicle has a generic axis-symmetric shape that is representative of Europe's lightweight VEGA launcher [5]. Having in mind its axisymmetry, the forces are expressed in the air-relative VRF as:

$$\mathbf{F}_{\text{aero,V}}(t) = -Q(t) S_{\text{ref}} \left[C_D \left(\alpha_{\text{eff}}(t), M(t) \right) \quad 0 \quad C_L \left(\alpha_{\text{eff}}(t), M(t) \right) \right]^{\text{T}} \tag{9}$$

where S_{ref} is a reference aerodynamic area and $\{C_D, C_L\}$ are the drag and lift coefficients, respectively. These coefficients are estimated from look-up tables as functions of the effective angle of attack $\alpha_{\text{eff}}(t)$ and Mach number $M(t) = \|\mathbf{v}_{\text{air}}(t)\| / a(t)$. The former is defined based on a small-angle assumption for the total angle of attack as follows:

$$\alpha_{\text{eff}}(t) = \sqrt{\alpha^2(t) + \beta^2(t)} \tag{10}$$

The aerodynamic force of Eq. (9) is thus written in the ECI frame as:

$$\mathbf{F}_{\text{aero,I}}(t) = C_{\mathbf{q}_{\text{I}}^{\text{B}}}(t) C_{\mathbf{q}_{\text{B}}^{\text{V}}}(t) \mathbf{F}_{\text{aero,V}}(t) \tag{11}$$

In addition, for the equations of motion, it is assumed that the aerodynamic moment generated around the vehicle's CG is only caused by the offset between this point and the centre of pressure (CP), where aerodynamic forces are applied. Hence, the aerodynamic moment is directly expressed in the body-fixed frame as:

$$\mathbf{M}_{\text{aero,B}}(t) = \left[\mathbf{x}_{\text{CP}}(t) - \mathbf{x}_{\text{CG}}(t) \right] \times C_{\mathbf{q}_{\text{B}}^{\text{V}}}(t) \mathbf{F}_{\text{aero,V}}(t) \tag{12}$$

In this equation, vectors $\mathbf{x}_{\text{CP}}(t) = [x_{\text{CP}}(t); 0; 0]$ and $\mathbf{x}_{\text{CG}}(t) = [x_{\text{CG}}(t); y_{\text{CG}}(t); z_{\text{CG}}(t)]$ represent respectively the CP and CG positions with respect to the same reference point in the body-fixed frame. Similar to the drag and lift coefficients, x_{CP} is computed from look-up tables as a function of $\alpha_{\text{eff}}(t)$ and $M(t)$, while the evolution of $\mathbf{x}_{\text{CG}}(t)$ is estimated (see Sec. 2.6).

Aerodynamic coefficients during the ascent flight are computed up to a 10 degree angle of attack based on the full vehicle's configuration. For the descent flight, aerodynamic coefficients are sparsely computed over the whole envelope based on the vehicle's first stage configuration.

Finally, it is also essential to have an idea of the thermal environment encountered by the RLV throughout L&R. A simple way to achieve this is by analysing the heat flux at the vehicle's stagnation point [22]. Given a reference nose radius R_{ref}, the maximum heat rate can be approximated by the Sutton Graves equation:

$$Q_H(t) = k_H \sqrt{\frac{\rho(t)}{R_{\text{ref}}}} \|\mathbf{v}_{\text{air}}(t)\|^3 \tag{13}$$

with $k_H \approx 1.74 \times 10^{-4}$ for Earth.

2.3 Thrust Vector Control

The vehicle's ascent and descent trajectories are controlled by adjusting the magnitude and direction of the thrust vector generated by its rocket engine. This adjustment is achieved via two TVC actuators that deflect the engine's nozzle by $\{\beta_{TVC,y}(t), \beta_{TVC,z}(t)\}$ along the body $\mathbf{j}_B$ and $\mathbf{k}_B$ axes respectively.

The required thrust magnitude $T_{ref}(t)$ and direction are commanded by the guidance subsystem (Sec. 3), with the latter using vehicle attitude reference angles $\{\phi_{ref}(t), \theta_{ref}(t), \psi_{ref}(t)\}$ as a surrogate. This decoupling between translational and rotational dynamics is common practice and often a good approximation since the vehicle's attitude can be changed considerably faster than its trajectory.

With this in mind, the TVC-generated force becomes:

$$\mathbf{F}_{TVC,B}(t) = T_{ref}(t) \begin{bmatrix} \cos\beta_{TVC,y}(t) \cos\beta_{TVC,z}(t) \\ \cos\beta_{TVC,y}(t) \sin\beta_{TVC,z}(t) \\ -\sin\beta_{TVC,y}(t) \end{bmatrix} \tag{14}$$

$$\mathbf{F}_{TVC,I}(t) = C_{\mathbf{q}_I^B}(t)\, \mathbf{F}_{TVC,B}(t) \tag{15}$$

and, with $\mathbf{x}_{PVP} = [x_{PVP}; 0; 0]$ representing the TVC pivot position, the moment around the CG is given by:

$$\mathbf{M}_{TVC,B}(t) = [\mathbf{x}_{PVP} - \mathbf{x}_{CG}(t)] \times \mathbf{F}_{TVC,B}(t) \tag{16}$$

The generation of thrust then causes the depletion of propellant. In this case, assuming negligible engine back-pressure losses, the mass-depletion dynamics is given by the rocket equation [15]:

$$\dot{m}(t) = -\frac{1}{I_{sp}g_0}\, T_{ref}(t) \tag{17}$$

where I_{sp} is the specific impulse of the engine and $g_0 \approx 9.81$ m/s^2 is the gravitational acceleration at the Earth's surface.

Recovering the launch vehicle requires the use of a re-ignitable and throttleable rocket engine. Here, a liquid engine using highly-refined kerosene (RP-1) as fuel and liquid oxygen (LOX) as oxidizer is adopted. This type of engine is common among many launcher manufacturers [16], including SpaceX [10]. Its main characteristics are summarised in Table 1a.

Vacuum specific impulse (s)	282
Oxidizer/fuel mass ratio	2.56
Oxidizer/fuel density ratio	1.42
Initial fuel mass (kg)	25913
Initial oxidizer mass (kg)	66337

(a) Engine

	Dry first stage	Payload total
Mass (kg)	2750	43000
CG Height (m)	4.60	12.91
MoI Axial (kg m^2)	3981	44000
MoI Lateral (kg m^2)	40267	3×10^6

(b) Structure

Table 1: Main RLV characteristics

In this table, the required initial propellant masses have been determined based on the mission under analysis and on information from the VEGA launcher [5]. In order for the tanks to meet VEGA's dimensions and initial MCI properties while ensuring that the remaining propellant after launch is enough for a powered descent, this results in a structural mass lower than the original one and in propellant densities higher than the actual LOX/RP engine. Nevertheless, the same density ratio of Table 1a is kept so as to have a meaningful representation of the CG travel throughout the burn. Further details on the launcher's MCI evolution are provided in Sec. 2.6.

2.4 Fins

Fin actuators are also included in the RLV model to ensure enough control authority under low (or zero) TVC effectiveness. This will be particularly critical throughout the descent flight, and thus they should be ideally placed above the vehicle's centre of pressure during this phase for improved stability. Here, only two pairs of fins are considered, but the generalisation in case additional surfaces are exploited for improved controllability is straightforward.

One pair of fins is then assigned to pitch motion control using deflections $\{\beta_{\mathrm{fin},1}(t), \beta_{\mathrm{fin},2}(t)\}$, the other pair to yaw control via $\{\beta_{\mathrm{fin},3}(t), \beta_{\mathrm{fin},4}(t)\}$ and it is assumed that any roll perturbation is rejected by the attitude control system so that the two pairs always remain in the trajectory yaw and pitch planes, respectively.

It is further assumed that, due to the reduced fin area compared to the RLV body, their axial force contribution is negligible so that only the normal component is accounted for and that this contribution has a sinusoidal dependence on the fin angle of attack given by:

$$C_{\mathrm{fin}}\left(\alpha_{\mathrm{fin}}(t)\right) = \bar{C}_{\mathrm{fin}} \sin \alpha_{\mathrm{fin}}(t) \tag{18}$$

where $\bar{C}_{\mathrm{fin}}$ is the maximum normal fin force coefficient and $\alpha_{\mathrm{fin}}(t)$ is the local angle of attack. The impact of these assumptions will be verified at a later stage through the consideration of aerodynamic uncertainties in the model.

The ith fin's angle of attack and its associated force in the RLV body-fixed frame $\mathbf{F}_{\mathrm{fin},i}(t)$ are then defined in the pitch plane:

$$\begin{cases} \alpha_{\mathrm{fin},i}(t) = \beta_{\mathrm{fin},i}(t) - \alpha(t) & i = \{1,2\} \\ \mathbf{F}_{\mathrm{fin},i}(t) = Q(t)S_{\mathrm{fin}}C_{\mathrm{fin}}\left(\alpha_{\mathrm{fin},i}(t)\right)\left[-\sin\beta_{\mathrm{fin},i}(t) \quad 0 \quad \cos\beta_{\mathrm{fin},i}(t)\right]^{\mathrm{T}} \end{cases} \tag{19}$$

and in the yaw plane as:

$$\begin{cases} \alpha_{\mathrm{fin},i}(t) = -\beta_{\mathrm{fin},i}(t) - \beta(t) & i = \{3,4\} \\ \mathbf{F}_{\mathrm{fin},i}(t) = Q(t)S_{\mathrm{fin}}C_{\mathrm{fin}}\left(\alpha_{\mathrm{fin},i}(t)\right)\left[\sin\beta_{\mathrm{fin},i}(t) \quad \cos\beta_{\mathrm{fin},i}(t) \quad 0\right]^{\mathrm{T}} \end{cases} \tag{20}$$

where S_{fin} is the surface area of one fin and $\alpha(t)$, $\beta(t)$ and $Q(t)$ are from Sec. 2.2. With this in mind, the fin-generated force in the ECI frame and the moment in the body frame correspond to:

$$\mathbf{F}_{\text{fins,I}}(t) = C_{\mathbf{q}_I^B}(t) \sum_{i=1}^{4} \mathbf{F}_{\text{fin},i}(t) \tag{21}$$

$$\mathbf{M}_{\text{fins,B}}(t) = \sum_{i=1}^{4} \left[\mathbf{x}_{\text{fin},i} - \mathbf{x}_{\text{CG}}(t) \right] \times \mathbf{F}_{\text{fin},i}(t) \tag{22}$$

where the CP of fin i, $\mathbf{x}_{\text{fin},i}$ is assumed to coincide with its geometric centre and can be read from Fig. 2.

For the rest of this study, $\bar{C}_{\text{fin}}$ has been fixed to 6, which is a reasonable value among conventional symmetrical airfoils, and S_{fin} has been set to 0.54 m^2 based on preliminary controllability analyses.

2.5 Cold Gas Thrusters

In addition, cold gas thrusters are included for controllability under zero main engine thrust and low fin effectiveness, which is the case at high altitudes where air density is very low.

Similar to the fins, a different pair of thrusters is assigned to pitch and yaw control. The force generated in the ECI frame is given by:

$$\mathbf{F}_{\text{thr,I}}(t) = C_{\mathbf{q}_I^B}(t) \, \bar{T}_{\text{thr}} \left(\beta_{\text{thr,y}}(t) \, \mathbf{k}_B - \beta_{\text{thr,z}}(t) \, \mathbf{j}_B \right) \tag{23}$$

where $\bar{T}_{\text{thr}}$ is the maximum thruster force and $\{\beta_{\text{thr,y}}(t), \beta_{\text{thr,z}}(t)\}$ are attitude commands about the body $\mathbf{j}_B$ and $\mathbf{k}_B$ axes, normalised between $[-1, 1]$. Equivalently, the corresponding moment in the body-fixed frame is:

$$\mathbf{M}_{\text{thr,B}}(t) = \bar{T}_{\text{thr}} \left(\left[\mathbf{x}_{\text{thr,y}} - \mathbf{x}_{\text{CG}}(t) \right] \times \beta_{\text{thr,y}}(t) \, \mathbf{k}_B - \left[\mathbf{x}_{\text{thr,z}} - \mathbf{x}_{\text{CG}}(t) \right] \times \beta_{\text{thr,z}}(t) \, \mathbf{j}_B \right) \tag{24}$$

In this equation, $\mathbf{x}_{\text{thr,y}}$ and $\mathbf{x}_{\text{thr,z}}$ represent the position of the thruster that is triggered for pitch and yaw control, which has to be adjusted in accordance with the sign of $\beta_{\text{thr,y}}(t)$ and $\beta_{\text{thr,z}}(t)$ (since commands in opposite directions trigger thrusters in opposite sides of the vehicle). In addition, $\bar{T}_{\text{thr}}$ is fixed to 400 N, which is a reasonable value among conventional actuators.

It is also important to note that, although there is a mass budget and depletion associated to cold gas thrusters, it is assumed to be negligible compared to that of the main engine.

2.6 Mass, CG & Inertia Evolution

In line with all the considerations above, the launcher configuration adopted is detailed in Fig. 2, showing the full vehicle on the left and the reusable first stage on the right. Since this study is focused on the ascent and descent flight of the first stage

only, all the other vehicle bodies (e.g. upper stages) will be referred to as payload (PL) from the perspective of the first stage. The vehicle is assumed to have an axis-symmetric shape and a uniform material (dry) density, with more mass allocated to the bottom and middle sections to account for the weight of the main engine module, retractable landing gear and inter-tank adapter. Moreover, it is assumed that fuel and oxidizer tanks are pressurised so as to maintain propellant masses at the bottom, which are then modelled as cylinders in end-burn, see [13].
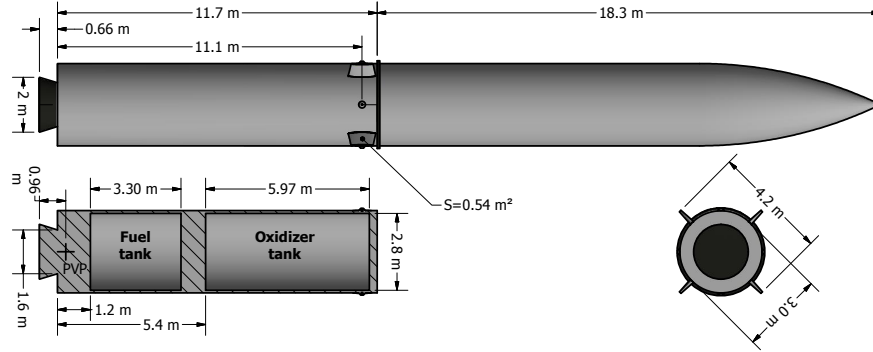

Fig. 2: Generic RLV and first stage

The MCI properties of the dry first stage and payload are summarised in Table 1b. In this table, and for the remainder of this section, heights are measured with respect to the first stage body base (i.e. 0.66 m above the nozzle exit), and moments of inertia (MoI) are relative to the CG of the corresponding body.

Based on this configuration, the vehicle's mass, which is updated via Eq. (17) during engine burn, breaks down into:

$$m(t) = m_{\text{prop}}(t) + m_{\text{dry}} + m_{\text{PL}} \tag{25}$$

with m_{dry} and m_{PL} in Table 1b and propellant mass $m_{\text{prop}}(t) = m_{\text{fuel}}(t) + m_{\text{oxid}}(t)$. Note that m_{PL} must be set to 0 after separation.

In order to compute the change over time of fuel and oxidizer masses, $m_{\text{fuel}}(t)$ and $m_{\text{oxid}}(t)$, as well as their level on the corresponding tank, $h_{\text{fuel}}(t)$ and $h_{\text{oxid}}(t)$, it is useful to normalise the propellant mass with respect to the initial values of Table 1a:

$$\eta(t) = \frac{m_{\text{prop}}(t)}{m_{\text{prop}}(0)}; \qquad m_{\#}(t) = \eta(t) m_{\#}(0); \qquad h_{\#}(t) = \eta(t) d_{\text{tk},\#} \tag{26}$$

where $\# = \{\text{fuel}, \text{oxid}\}$, $d_{\text{tk,fuel}}$ (3.30 m) and $d_{\text{tk,oxid}}$ (5.97 m) are the tank depths depicted in Fig. 2.

Due to propellant mass and level variations, the total vehicle CG and MoI vary substantially throughout the flight. In the nominal case, the former lies along the body longitudinal axis, $\mathbf{x}_{\text{CG}}(t) = [x_{\text{CG}}(t); 0; 0]$, and is computed as:

$$x_{\text{CG}}(t) = \frac{1}{m(t)} \left[m_{\text{fuel}}(t) \left(h_{\text{tk,fuel}} + \frac{h_{\text{fuel}}(t)}{2} \right) + \right.$$
$$\left. + m_{\text{oxid}}(t) \left(h_{\text{tk,oxid}} + \frac{h_{\text{oxid}}(t)}{2} \right) + m_{\text{dry}} h_{\text{dry}} + m_{\text{PL}} h_{\text{PL}} \right] \tag{27}$$

where $h_{\text{tk,fuel}}$ (1.2 m) and $h_{\text{tk,oxid}}$ (5.4 m) are the tank heights provided in Fig. 2 and h_{dry} and h_{PL} are given in Table 1b.

Based on the same assumptions, the inertia tensor is diagonal in nominal conditions and expressed as $J(t) = \text{diag}\,[J_A(t); J_N(t); J_N(t)]$. The axial component corresponds directly to:

$$J_A(t) = \frac{1}{2} m_{\text{prop}}(t)\, r_{\text{tk}}^2 + J_{A,\text{dry}} + J_{A,\text{PL}} \tag{28}$$

in which r_{tk} (1.4 m) is the tank radius. The lateral contributions of propellant masses relative to their CG are given by:

$$J_{N,\#}(t) = \frac{1}{12} m_{\#}(t) \left(3 r_{\text{tk}}^2 + h_{\#}^2(t) \right) \tag{29}$$

with $\# = \{\text{fuel, oxid}\}$, and all the contributions are converted to vehicle's CG coordinates using the parallel axis theorem as follows:

$$J_N(t) = J_{N,\text{fuel}}(t) + J_{N,\text{oxid}}(t) + J_{N,\text{dry}} + J_{N,\text{PL}} +$$
$$+ m_{\text{fuel}}(t) \left(h_{\text{tk,fuel}} + \frac{h_{\text{fuel}}(t)}{2} - x_{\text{CG}}(t) \right)^2 + m_{\text{oxid}}(t) \left(h_{\text{tk,oxid}} + \frac{h_{\text{oxid}}(t)}{2} - x_{\text{CG}}(t) \right)^2 +$$
$$+ m_{\text{dry}} \left(h_{\text{dry}} - x_{\text{CG}}(t) \right)^2 + m_{\text{PL}} \left(h_{\text{PL}} - x_{\text{CG}}(t) \right)^2 \tag{30}$$

Once again, m_{PL}, $J_{A,\text{PL}}$ and $J_{N,\text{PL}}$ are set to 0 after separation and $x_{\text{CG}}(t)$ is computed via Eq. (27).

3 RLV Guidance Approach

This section provides a general introduction of reference mission profile and booster-back recovery strategies (Sec. 3.1), followed by the description of the convex optimisation-based *DESCENDO* algorithm (Sec. 3.2).

3.1 Launch & Recovery Mission Profiles

In recent years, several studies [9, 8, 31, 26, 12] have addressed the problem of RLV performance optimisation. These are mostly focused on the application of multi-disciplinary optimisation (MDO) methods to determine L&R trajectories that allow delivering the highest payload while fulfilling competing mission and aerothermal

load requirements. In contrast, the present study is not focused on the optimisation of payload capabilities, but rather on analysing the practical feasibility of different descent trajectories, together with the impact of different G&C choices on the aerothermal loads encountered during the flight and on recovery performance.

For the above reason, the launch mission profile and the vehicle configuration described here remain fixed throughout this study and only the recovery trajectory is modified. The ascent profile corresponds to that of a 1,100 kg satellite injection in a quasi-polar orbit at an altitude of 800 km using an expendable solid-propellant launcher from the European Space Centre in French Guiana. Concerning its recovery, two distinct strategies are addressed and discussed below: downrange landing (DRL) and return to launch site (RTLS), see Fig. 3.
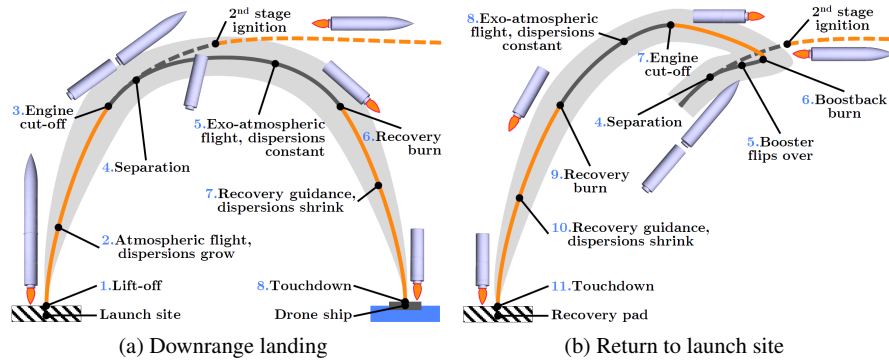

Fig. 3: Recovery mission profiles

The most straightforward booster-back recovery strategy is known as downrange landing (DRL). In this scenario, the idea is for the reusable stage to be landed close to its un-propelled impact site, therefore minimising the propellant required for the landing. However, launches typically take place in the direction of the sea due to safety reasons, thus a sea-going recovery platform needs to be placed at the landing point and then bring the stage back. This approach has been successfully employed by SpaceX [6], which uses a 91 m by 52 m drone ship as recovery pad.

From Fig. 3a, DRL missions start naturally with lift-off and ascent of the first stage (points 1 and 2 in the figure). This part of the mission is typically flown with open-loop guidance, hence dispersions due to system uncertainties and environmental perturbations tend to grow. These dispersions are then compensated for by the exo-atmospheric stages in order to ensure an accurate satellite injection. Open-loop guidance commands are provided in terms of reference attitude angles $\{\theta_{\text{ref}}(t), \psi_{\text{ref}}(t)\}$ relative to the LP frame and thrust magnitude $T_{\text{ref}}(t)$.

After 110 seconds of flight, the first stage cuts off its engine and separates two seconds after (points 3 and 4 of Fig. 3a). The second stage then ignites its engine and proceeds the flight towards the payload's destination orbit. In the meantime (point 5), the first stage continues its exo-atmospheric motion in the direction of the recovery platform with approximately constant dispersions but with increasing velocity due to the action of gravity.

Then, at a pre-specified altitude h_s, the first stage re-ignites its engine for the recovery burn (point 6), which must be able to counteract dispersions (point 7) and bring the booster from its current position and velocity to a soft touchdown at the drone ship (point 8). The ability to cope with dispersions during recovery leads to the need for closed-loop guidance techniques, where guidance commands are computed in real-time to correct the trajectory based on onboard measurements. All the computations are made in the RP frame and the required thrust vector in this frame is then converted back to $\{\theta_{\text{ref}}(t), \psi_{\text{ref}}(t)\}$ and $T_{\text{ref}}(t)$.

Furthermore, for a more efficient management of aerothermal requirements, recovery guidance can be explicitly divided into three phases: (i) a re-entry burn aimed at decelerating the booster, (ii) a second engine cut-off and (iii) a landing burn that ensures a precise touchdown. In addition, as depicted in Fig. 3a, the reusable stage needs to undergo a significant change in attitude between points 4 and 6. This flip-over manoeuvre is simulated by a change in pitch with constant rate executed using fins and cold gas thrusters.

As an alternative recovery solution, the reusable booster can use its main engine not only for deceleration and landing, but also to deliver an additional burn that brings it to a recovery pad close to the launch site. The additional firing naturally leads to a more demanding propellant consumption, which can be nonetheless paid for by avoiding the use of a sea-going platform and all the associated infrastructure and operational costs. This recovery strategy is known as return to launch site (RTLS) and is illustrated in Fig. 3b.

Until separation (i.e. point 4), the RTLS and DRL missions have the same profile, which is therefore omitted in Fig. 3b for clarity. From this point forward, as introduced above, the reusable stage needs to perform a rapid flip-over manoeuvre (point 5) followed by the boostback burn (point 6) in the direction of the launch site. Following the boostback cut-off (point 7), the rest of the recovery (from point 8 onwards) is similar to DRL: an exo-atmospheric flight where the booster flips over at a slower rate, a closed-loop recovery stage that starts at h_s (and is achieved with one or two distinct burns), and finally a soft touchdown.

In the RTLS scenario, the flip-over manoeuvres are again executed by fin and thruster induced pitch variations with constant rate. In addition, for this study, the boostback burn is fixed to an open-loop firing with magnitude $T_{\text{ref}} = 600$ kN, direction $\{\theta_{\text{ref}}, \psi_{\text{ref}}\} = \{180, 0\}$ degrees and duration 30 seconds.

Finally, it is important to mention that closed-loop guidance techniques for powered descent and landing are generally independent of the type of recovery strategy – since all the computations are made in the RP frame, the only difference lies on the definition of this frame and of the corresponding transformation.

3.2 The DESCENDO algorithm

Convex optimisation guidance is based on solving a fuel-optimal trajectory generation problem with state and control constraints. This problem is typically nonlinear and challenging to solve and, until the past decade, its application was only feasible in an offline setting (where open-loop trajectories are designed on the ground with powerful computers). However, mathematical and computational developments in recent years have enabled representative solutions to be determined online using

onboard computers and applied in a closed-loop fashion. This shift has been coined *computational guidance and control* [27] and has been demonstrated experimentally [3, 23] and at a commercial level by companies like SpaceX and Blue Origin.

The most relevant mathematical development allowing this paradigm is known as *lossless convexification* [4, 7]. This procedure allows to reformulate non-convex constraints in a convex (CVX) form and modify the problem into a second-order cone program (SOCP), for which powerful interior-point solvers exist. The optimal solution of the relaxed program then recovers the optimal solution of the original problem. In addition, a technique known as *successive convexification* [19, 18] can be applied to eliminate any remaining nonlinearities such as aerodynamic effects. This technique constitutes an iterative process in which the nonlinearities are repeatedly approximated using information from the previous solution.

The powered landing algorithm developed in this study is based on the work of *Szmuk et al.* [30] and *Jerez et al.* [17], with a few fundamental and critical differences. The latter reference [17] is mostly focused on maximising computational efficiency and, although ideal for real-time execution, it relies on an extensive simplification of the equations of motion including disregarding the aerodynamic forces, which play a decisive role in the vehicle's recovery trajectory. On the other hand, the former reference [30] takes a completely different approach and focuses on maximising the optimality of the solution by employing successive convexifications to account for aerodynamic effects (as well as engine back-pressure losses). It is also noted that the two approaches have only been verified for low-altitude and low-velocity flight and that the assumption of constant air density made in *Szmuk et al.* [30] is not physically representative of RLVs.

With this in mind, the objective of the algorithm proposed in this article is to attain a middle ground between the efficiency and optimality of the two aforementioned approaches that is suitable for the extended flight envelope encountered by the RLV. This algorithm is then termed *DESCENDO* (Descending over Extended Envelopes using Successive Convexification-based Optimisation). One additional difference with respect to *Szmuk et al.* [30] is that the touchdown time t_f is not an optimisation variable and needs to be specified. This choice is made in order to provide a common comparative framework with other state-of-the-art techniques.

The *DESCENDO* guidance algorithm is schematised in Fig. 4 and briefly described below. Further details are available in [24]. The algorithm is implemented in MATLAB using the CVX library [14] to formulate the convex problems, and the ECOS routine [11] to solve them.

The proposed algorithm consists of two SOCP stages, see Fig. 4: SOCP 1, which allows to find a discrete thrust acceleration, and SOCP 2 where successive convexifications are iteratively applied to define a convex approximation of the aerodynamic effects. Then, at each simulation step, the final solution serves to determine (via linear interpolation) the commanded thrust vector in the RP frame $\mathbf{T}_{\text{CVX}}(t)$. This solution is stored as an online look-up table and updated only when a SOCP is executed and a feasible solution is found. SOCPs are triggered at every guidance step under a pre-specified altitude h_{S}. The frequency of guidance steps is smaller than the simulation rate, $f_{\text{gui}} < f_{\text{sim}}$, and represents a trade-off between guidance performance and computational load.

At each guidance step, optimisation variables are discretised into N equally-spaced points, ranging from the current instant of time t to touchdown time t_f. The interval of time between two consecutive points corresponds to:

$$T_{\mathrm{S}} = \frac{t_f - t}{N - 1} \tag{31}$$

and, since $T_{\mathrm{S}} \to 0$ as $t \to t_f$, the accuracy of the discretisation becomes more refined towards the end-of-mission.
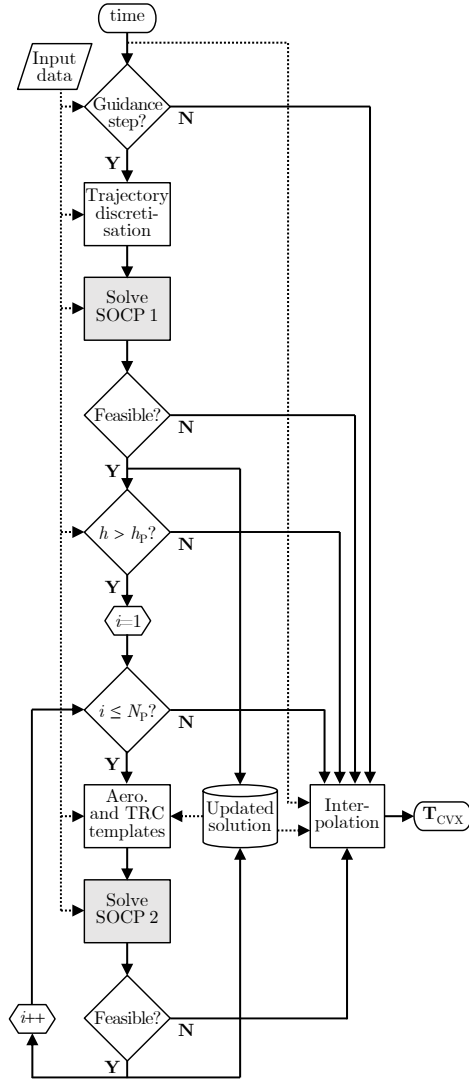

Fig. 4: *DESCENDO* guidance algorithm

In addition, to achieve lossless convexification, the following changes of variables are introduced:

$$\mathbf{w}(t) = \frac{\mathbf{T}_{\mathrm{CVX}}(t)}{\hat{m}(t)}; \qquad \sigma(t) = \frac{\|\mathbf{T}_{\mathrm{CVX}}(t)\|}{\hat{m}(t)}; \qquad z(t) = \ln \hat{m}(t) \qquad (32)$$

Using this setup, the objective of the first SOCP is to find a discrete thrust acceleration profile $\mathbf{w}[k]$ ($k \in [1, \cdots, N]$) that minimises the vehicle's fuel consumption, which is equivalent to maximising its final mass or $z[N]$. The SOCP 1 formulation is characterised by the use of dynamic equations to describe mass depletion and translational motion, the use of surrogate variables for the lossless convexification method and vehicle acceleration, and the use of the following main constraints:

- Boundary conditions including final vertical velocity $\mathbf{v}_z[N]$ and thrust acceleration vector $\mathbf{w}[N]$;
- Control constraints on thrust direction and magnitude during burn periods;
- Control rate constraints.

The main limitation of this formulation lies on its inability to account for aerodynamic forces. Without any knowledge of the deceleration caused by these forces, the algorithm will always overestimate the propellant required for the recovery and provide an inadequate guidance solution. Furthermore, because of this discrepancy, the inclusion of additional specifications such as flight path constraints becomes superfluous.

To overcome the aforementioned limitations, the *DESCENDO* algorithm then introduces the successive convexification procedure of references [19, 18]. This involves solving a second (iteratively more refined) SOCP in which the solution of the previous problem is employed to define a *convex approximation* of the aerodynamic effects. This cycle is executed a limited number of times N_{P} *per guidance step* and the solution of SOCP 1 (if feasible) is used for the first iteration. This results in $N_{\mathrm{P}} + 1$ SOCPs being solved at each guidance step.

Aerodynamic effects in the refined SOCP are approximated by augmenting the surrogate acceleration vector with a velocity-dependent term that accounts for the deceleration due to aerodynamic drag.

In addition to the aerodynamic template, the iterative process includes a condition that ensures the algorithm's convergence by bounding the deviation between guidance solutions found in two consecutive iterations. This condition is known as *trust region constraint* (TRC) and defined as:

$$\|\mathbf{w}[k] - \mathbf{w}_i^*[k]\| \leq \eta_{\mathbf{w}}[k] \qquad (33)$$

where $\mathbf{w}_i^*[k]$ is the thrust acceleration template determined by the previous SOCP iteration. The TRC is enforced by minimising $\eta_{\mathbf{w}}[k]$, hence the SOCP objective function needs to be augmented with the point-wise sum of this vector, weighted by $w_{\eta_{\mathbf{w}}}$. A smaller value of $w_{\eta_{\mathbf{w}}}$ will be reflected in a larger variation between solutions and vice-versa.

Comparing this problem with SOCP 1, two increasingly stringent specifications are made: (i) the inequality relaxation of $\mathbf{v}_z[N]$ is dropped, and (ii) a flight path constraint is introduced in $\mathbf{r}[k]$. In addition to subsurface flight avoidance, the latter constraint ensures that the recovery trajectory remains in the interior of a cone with vertex at the landing point and with the vehicle's current position $\hat{\mathbf{r}}(t)$ on its surface.

It is also important to note that, as evidenced in Fig. 4, SOCP 2 is only solved while the vehicle is higher than a pre-specified altitude h_{P}. The reason for this is related to the fact that velocity is significantly smaller at low altitudes and

thus aerodynamic forces become less intense. Therefore, disregarding their impact here introduces less error while reducing the overall computational time. Furthermore, this choice allows to prevent a singularity in the flight path constraint when $\|\hat{\mathbf{r}}_{x,y}(t)\| \to 0$.

4 Simulation Results

This section provides a coupled flight mechanics and guidance analysis of an RTLS mission using the *DESCENDO* algorithm for recovery and a perfect attitude control assumption. This means that attitude angles are exactly what they are commanded to be and that all the aerodynamic moments generated by the vehicle are compensated for, which represents the standard approach for developing and assessing guidance schemes. Additional analyses without this assumption and for a DRL mission are available in [25, 24].

Detailed simulation results with $h_s = 25$ km and $t_f = 380$ s are plotted in Fig. 5. The phases of launch (from lift-off to separation), exo-atmospheric flight (from separation to recovery burn) and recovery (from recovery burn to touchdown) are distinguished in every plot using dash-dotted, dashed and continuous lines respectively.
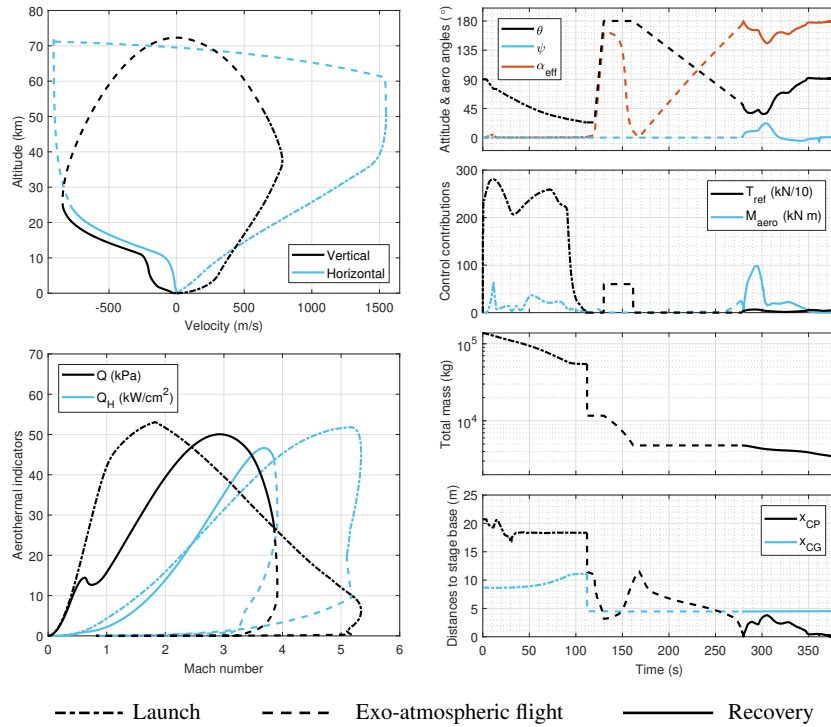

Fig. 5: RTLS flight mechanics results using *DESCENDO*

The top-left plot of Fig. 5 shows the evolution of vertical and horizontal velocity as a function of altitude (in the vertical axis). During launch, velocity increases in both vertical and horizontal directions and separation occurs when the latter reaches its maximum value at an approximate altitude of 51 km. From that point, the vehicle continues to ascent until its vertical velocity becomes zero at an approximate altitude of 72 km and then starts to accelerate downwards due to the action of gravity. In the meantime, the boostback burn results in the inversion of the horizontal component and reduction of its magnitude to approximately half of its value at separation. Then, at 25 km, recovery guidance is activated and the commanded burn brings both components to zero at the landing point. It is important to notice that horizontal velocity converges to this value significantly before their counterpart, which is critical to ensure a vertical landing.

The bottom-left plot illustrates the evolution of dynamic pressure (Eq. (6)) and heat flux (Eq. (13)) as a function of the vehicle's Mach number. During launch, velocity increases and air density decreases, which causes Q and Q_H to tend to zero at lift-off and at maximum altitude (where $M \approx 5.3$) and to have a peak value in-between. These indicators then increase abruptly once the RLV plunges downwards (at $M \approx 3.9$) and re-enters the atmosphere. At this point, recovery guidance is activated in order to manage the second peak value of these indicators and bring it to zero at the landing point.

The uppermost plot on the right-hand side of Fig. 5 shows the reference pitch and yaw angles $\{\theta_{\mathrm{ref}}, \psi_{\mathrm{ref}}\}$ as well as the total angle of attack α_{eff} over mission time. Lift-off, pitch over and gravity turn manoeuvres are clearly identified in the pre-programmed angles during launch and, in terms of angle of attack, during this phase it remains close to zero with a maximum value under 5 degrees around the pitch over phase. Subsequently, the reference pitch angle undergoes a rapid flip over manoeuvre, followed by a 30 seconds period with constant pitch during which the boostback burn takes place (recall Fig. 3b) and by a second constant-rate manoeuvre prior to the recovery burn. The flip over manoeuvre causes the total angle of attack to follow the pitch variation, but the former angle returns to zero as soon as the horizontal velocity is inverted by the boostback burn. Finally, during the recovery, the reference attitude angles are computed by the guidance algorithm, which results in θ_{ref} converging to 90 degrees at touchdown, ψ_{ref} remaining close to zero (due to little aerodynamic couplings with the pitch motion) and α_{eff} close to 180 degrees.

The second right-hand plot illustrates the evolution of the thrust vector magnitude T_{ref} and aerodynamic moment $||\mathbf{M}_{\mathrm{aero}}||$. Similarly to the previous plot, T_{ref} is pre-programmed for launch and computed online by the guidance algorithm during recovery. The reference associated with the boostback burn is also clearly visible. The aerodynamic moment to be compensated, as expected, is more demanding in zones of high dynamic pressure and angle of attack.

The third right-hand plot plot on the right-hand side of Fig. 5 shows the evolution of the vehicle's total mass using logarithmic scale for clarity. Here, four mass-depletion zones can be identified: launch burn, separation (sudden drop of m_{PL} at 112 seconds of flight), boostback and recovery burn. In this scenario, while 90.35% of propellant is depleted during launch, 8.95% is required for the recovery, which leaves a margin of about 0.7%.

Finally, the bottom-right plot illustrates the longitudinal travel of CP and CG (relative to the booster's base) throughout the flight. While the former is governed by the aerodynamic environment encountered, the latter follows the depletion of mass

as per Eq. (27). Hence, the same mass-depletion zones exist, although post-launch variations cannot be distinguished as changes in mass are comparatively small. In any case, the RLV is inherently unstable during powered flight since the CP is located in front of the CG during ascent and behind it during descent.

The performance indicators analysed throughout this section (i.e. aerothermal loads, propellant consumption, touchdown errors, etc.) should be ideally as small as possible. However, in practice, configuration or mission choices that optimising one of them (e.g. propellant) will likely worsen others (e.g. aerodynamic pressure), and substantial improvements can only be achieved through more sophisticated guidance and control. Although not shown in this article, it has been verified that, in contrast to other state-of-the-art guidance techniques, the *DESCENDO* algorithm enables combined improvements of all the indicators due to the efficient consideration of aerodynamic effects during descent.

5 Conclusions

The optimisation of reusable launcher flight performance while meeting tight aerodynamic and thermal load constraints is a challenging problem. Significant benefits can be achieved by jointly addressing the two tasks of dimensioning and design but, in order to do this, a complete revision of the current process for launchers must be performed to manage the more complex process of reusable launchers.

In this article, a flight mechanics model of a reusable launch vehicle has been developed to study and address the critical coupling between guidance and control. It incorporates the main critical components for studying such effects, although some standard simplifying assumptions have been used. Despite these assumptions, the validity of the benchmark has been exemplified through the design and verification of a novel recovery guidance algorithm termed *DESCENDO. DESCENDO* is a successive convexification-based method aimed at providing a balance between computational efficiency and trajectory optimality that is suitable for the extended flight envelope encountered by reusable launchers.

References

1. *U.S. Standard Atmosphere*. NASA Technical Reports Server, Oct 1976.
2. *MATLAB Aerospace Toolbox User's Guide*. MathWorks, 23rd edition, September 2017.
3. B. Açikmeşe, M. Aung, J. Casoliva, S. Mohan, A. Johnson, D. Scharf, D. Masten, A. Scotkin, S. Wolf, and M. Regehr. Flight Testing of Trajectories Computed by G-FOLD: Fuel Optimal Large Divert Guidance Algorithm for Planetary Landing. In *The 23rd AAS/AIAA Spacefilght Mechanics Meeting*, Kauai, HI, Feb 10–14 2013.
4. B. Açikmeşe and S. Ploen. Convex Programming Approach to Powered Descent Guidance for Mars Landing. *Journal of Guidance, Control, and Dynamics*, 30(5):1353–1366, 2007.
5. S. Bianchi. VEGA, the European small launcher: Development status, future perspectives, and applications. *Acta Astronautica*, 63:416–427, 2008.
6. L. Blackmore. Autonomous Precision Landing of Space Rockets. *The Bridge on Frontiers of Engineering*, 4(46):15–20, 2016.
7. L. Blackmore, B. Açikmeşe, and D. Scharf. Minimum-Landing-Error Powered-Descent Guidance for Mars Landing Using Convex Optimization. *Journal of Guidance, Control, and Dynamics*, 33(4):1161–1171, 2010.

8. J. Bradford, B. Germain, and K. Feld. Optimization of a Reusable Rocket-Powered, VTVL Launch System: A Case Study of the Falcon 9-R. *SpaceWorks Case Study*, Aug 2014.

9. J. Bradford and B. Hellman. Return to Launch Site Trajectory Options for a Reusable Booster without a Secondary Propulsion System. In *The AIAA SPACE 2009 Conference and Exposition*, Passadena, CA, Sep 14–17 2009.

10. A. Chinnery and G. Shotwell. Space Exploration Technologies' Falcon I Launcher: Towards Operationally Responsive Spacelift. In *The 40th AIAA/ASME/SAE/ASEE Joint Propulsion Conference and Exhibit*, Fort Lauderdale, FL, Jul 11–14 2004.

11. A. Domahidi, E. Chu, and S. Boyd. ECOS: An SOCP solver for embedded systems. In *The 2013 European Control Conference*, Zurich, Switzerland, Jul 17–19 2013.

12. E. Dumont, S. Stappert, T. Ecker, J. Wilken, S. Karl, S. Krummen, and M. Sippel. Evaluation of Future Ariane Reusable VTOL Booster Stages. In *The 68th International Astronautical Congress*, Adelaide, Australia, Sep 25–29 2017.

13. F. O. Eke. *Dynamics of Variable Mass Systems*. NASA Technical Reports Server, Jan 1998.

14. M. Grant and S. Boyd. CVX: Matlab Software for Disciplined Convex Programming, version 2.1. Online available at http://cvxr.com/cvx, 2014.

15. A. L. Greensite. *Analysis and Design of Space Vehicle Flight Control Systems*, volume II and VII. Spartan, 1970.

16. S. Isakowitz, J. Hopkins Jr., and J. Hopkins. *International Reference Guide to Space Launch Systems*. AIAA, 3rd edition, 1999.

17. J. Jerez, S. Merkli, S. Bennani, and Strauch. FORCES-RTTO: A Tool for On-board Real-time Autonomous Trajectory Planning. In *The 10th International ESA Conference on Guidance, Navigation and Control Systems*, Salzburg, Austria, May 29–Jun 2 2017.

18. X. Liu. Fuel-Optimal Rocket Landing with Aerodynamic Controls. In *The AIAA SciTech 2017 Forum*, Grapevine, TX, Jan 9–13 2017.

19. X. Liu and P. Lu. Solving Nonconvex Optimal Control Problems by Convex Optimization. *Journal of Guidance, Control, and Dynamics*, 37(3):750–765, 2014.

20. E. Mooij and D. Gransden. The Impact of Aeroelastic Effects on the Controllability of Conventional Launch Vehicles. In *The 67th International Astronautical Congress*, Guadalajara, Mexico, Sep 26–30 2016.

21. N. Pavlis, S. Holmes, S. Kenyon, and J. Factor. An Earth Gravitational Model to Degree 2160: EGM2008. In *The 2008 General Assembly of the European Geosciences Union*, Vienna, Austria, Apr 13–18 2008.

22. F. J. Regan and S. M. Anandakrishnan. *Dynamics of Atmospheric Re-Entry*. AIAA Education Series, 1993.

23. D. Scharf, M. Regehr, G. Vaughan, J. Benito, H. Ansari, M. Aung, A. Johnson, J. Casoliva, S. Mohan, D. Dueri, B. Açikmeşe, D. Masten, and S. Nietfeld. ADAPT Demonstrations of Onboard Large-Divert Guidance with a VTVL Rocket. In *The 2014 IEEE Aerospace Conference*, Passadena, CA, Mar 1–8 2014.

24. P. Simplício, A. Marcos, and S. Bennani. Guidance of Reusable Launchers: Improving Descent and Landing Performance. *submitted to the Journal of Guidance, Control, and Dynamics*, 2018.

25. P. Simplício, A. Marcos, and S. Bennani. Reusable Launchers: Development of a Coupled Flight Mechanics, Guidance and Control Benchmark. *submitted to the Journal of Spacecraft and Rockets*, 2018.

26. M. Sippel, S. Stappert, L. Bussler, and E. Dumont. Systematic Assessment of Reusable First-Stage Return Options. In *The 68th International Astronautical Congress*, Adelaide, Australia, Sep 25–29 2017.

27. Special Issue on Computational Guidance and Control. *Journal of Guidance, Control, and Dynamics*, 40(2), Feb 2017.

28. B. Starr, I. Yunis, and O. Aaron. Use of Flexible Body Coupled Loads in Assessment of Day of Launch Flight Loads. In *The 2011 AIAA Atmospheric Flight Mechanics Conference*, Portland, OR, Aug 8–11 2011.

29. M. Szmuk and B. Açikmeşe. Successive Convexification for 6-DoF Mars Rocket Powered Landing with Free-Final-Time. In *The AIAA SciTech 2018 Forum*, Kissimmee, FL, Jan 8–12 2018.

30. M. Szmuk, B. Açikmeşe, A. Berning Jr., and G. Huntington. Successive Convexification for Fuel-Optimal Powered Landing with Aerodynamic Drag and Non-Convex Constraints. In *The AIAA SciTech 2016 Forum*, San Diego, CA, Jan 4–8 2016.

31. P. Tartabini, J. Beaty, R. Lepsch, and M. Gilbert. *Payload Performance Analysis for a Reusable Two-Stage-to-Orbit Vehicle*. NASA Technical Reports Server, May 2015.